Synthesis

(lutH)[$Fe^{III}_{30}(\mu_4\text{-}O)_6(\mu_3\text{-}O)_{26}(\mu\text{-}OH)_{15}Br_9(lut)_{15}$]$Br_3$ (1)

$FeBr_3$ (0.591 g, 2 mmol) was dissolved with hexamethylenetetramine (0.476 g, 3.4 mmol) MeCN (25 ml) and 3,4-lutdine (0.35 ml, 3.1 mmol) was added. The reaction was stirred for four hours and then filtered and allowed to stand undisturbed overnight. Diffusion of iPrOH into this solution afforded dark brown plate-shaped crystals suitable for X-ray diffraction after 3 weeks. Yield $\leq$ 10%. Elemental analysis (% C H N) calculated (found) for $Br_{12}C_{112}Fe_{30}H_{159}N_{16}O_{47}$: C 26.30 (25.81), N 4.38 (3.62) H 3.13 (2.84).

(Et-PyH)[$Fe^{III}_{30}(\mu_4\text{-}O)_6(\mu_3\text{-}O)_{26}(\mu\text{-}OH)_{15}Br_9$(Et-py)$_{15}$]$Br_3$·Et-py (1a)

Synthesis as for compound **1**, replacing 3,4-lutidine (0.35 ml) with 4-ethylpyridine (1 ml, 8.8 mmol) and iPrOH with diethylether. Yield $\leq$ 10%. Elemental analysis (% C H N) calculated (found) for $Br_{12}C_{119}Fe_{30}H_{169}N_{17}O_{47}$: C 27.36 (26.72), N 4.56 (4.03) H 3.26 (2.95).

Single crystal X-ray crystallography

1. Single brown plate crystals of **1** were recrystallised from a mixture of acetonitrile and isopropanol by vapour diffusion. A suitable crystal with dimensions 0.15 × 0.12 × 0.04 mm^3 was selected and mounted on a MITIGEN holder in Paratone oil on a Diamond Light Source I-19 EH1 diffractometer. The crystal was kept at a steady T = 100.0 K during data collection. The structure was solved with the Superflip solution program using iterative methods and by using Olex2 as the graphical interface. The model was refined with ShelXL 2018/3 using full matrix least squares minimisation on F^2.[1,2]

1a. Single dark brown block-shaped crystals of **1a** were recrystallised from a mixture of diethyl ether and acetonitrile by vapour diffusion. A suitable crystal 0.17 × 0.09 × 0.06 mm^3 was selected and mounted on a MITIGEN holder in Paratone oil on an Rigaku Oxford Diffraction SuperNova diffractometer. The crystal was kept at a steady T = 120.0 K during data collection. The structure was solved with the ShelXT structure solution program using the Intrinsic Phasing solution method and by using Olex2 as the graphical interface. The model was refined with version 2018/3 of ShelXL using Least Squares minimisation.[1,2]

Table S1. Crystallographic information for **1** and **1a**.

Compound	**1**	**1a**
Formula	$Br_{12}C_{112}Fe_{30}H_{159}N_{16}O_{47}$	$C_{119}H_{169}Br_{12}Fe_{30}N_{17}O_{47}$
$D_{calc.}$/ g cm^{-3}	1.575	1.643
μ/mm^{-1}	3.885	19.117
Formula Weight	5115.96	5224.12
Colour	brown	dark brown
Shape	plate	block
Size/mm^3	0.15×0.12×0.04	0.17×0.09×0.06
T/K	100.0	120.0
Crystal System	monoclinic	triclinic
Space Group	*Pn*	*P*-1
Flack Parameter	0.159(10)	-
Hooft parameter	0.192(4)	-
a/Å	30.929(3)	20.7362(5)
b/Å	21.777(2)	22.7181(4)
c/Å	32.273(4)	25.0130(4)
α/°	90	95.425(2)
β/°	96.882(2)	97.928(2)
γ/°	90	113.427(2)
V/Å^3	21580(4)	10563.0(4)
Z	4	2
Z'	2	1
Wavelength/Å	0.6889	1.54178
Radiation type	Synchrotron	CuK_{α}
Θ_{min}/°	0.835	3.617
Θ_{max}/°	20.136	76.143
Measured Refl.	168652	174652
Independent Refl.	44728	43629
Reflections with I > 2(I)	32432	29952
R_{int}	0.0752	0.0982
Parameters	3442	2012
Restraints	9631	950
Largest Peak	0.614	1.506
Deepest Hole	-0.468	-1.245
GooF	1.038	0.984
wR_2 (all data)	0.1530	0.1791
wR_2	0.1405	0.1618
R_1 (all data)	0.0794	0.0890
R_1	0.0549	0.0633
CCDC	2105690	2105691

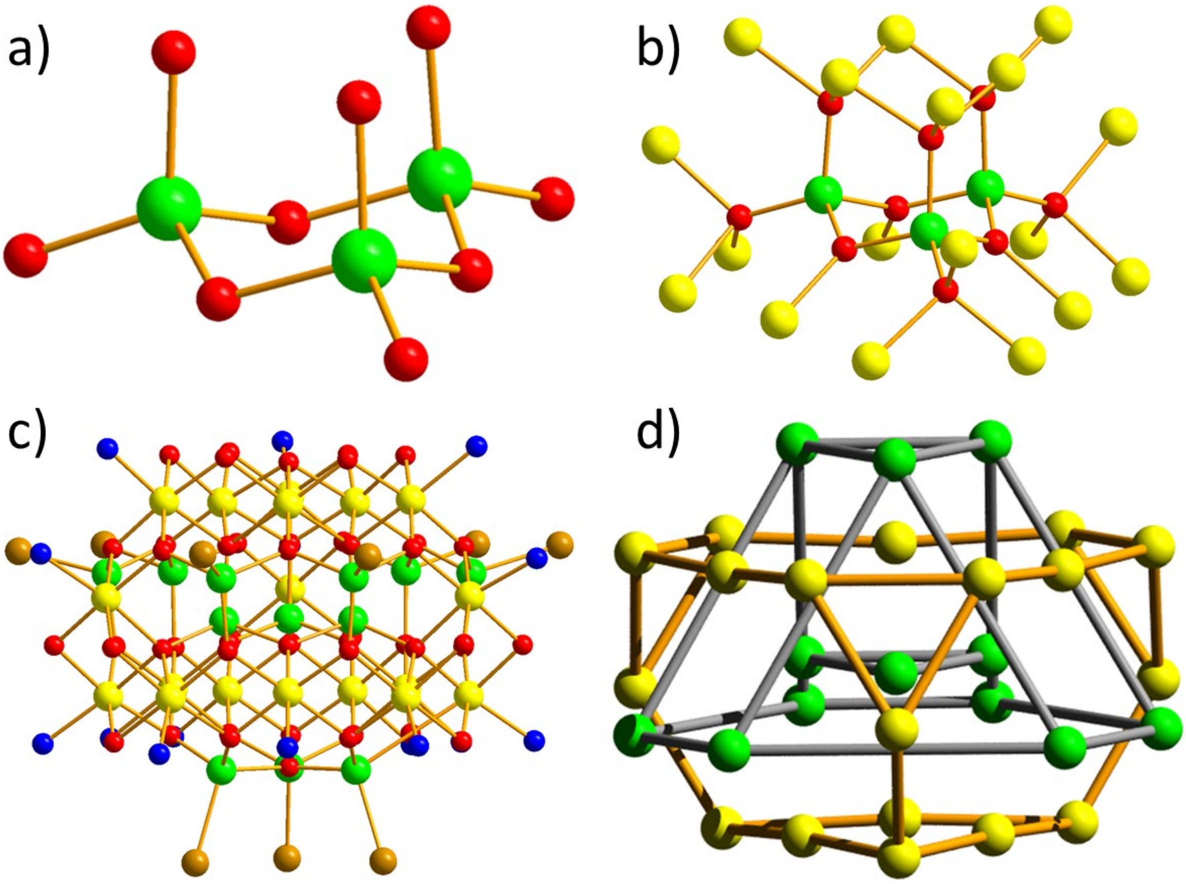

Figure S1. The metal-oxygen core in **1**, highlighting the inner $[Fe^{III}_3O_9]^{18-}$ triangle of tetrahedral Fe ions (a) linked to the $[Fe^{III}_{18}O_{22}]^{12+}$ unit of octahedral Fe ions (b), surrounded by the $[Fe^{III}_9]$ partial cuboctahedron of tetraherdal Fe ions (c). (d) Metallic skeleton. Colour code: tetrahedral Fe = green, octahedral Fe = yellow, O = red, N = blue, C = black, Br = brown. H atoms and anions omitted for clarity.

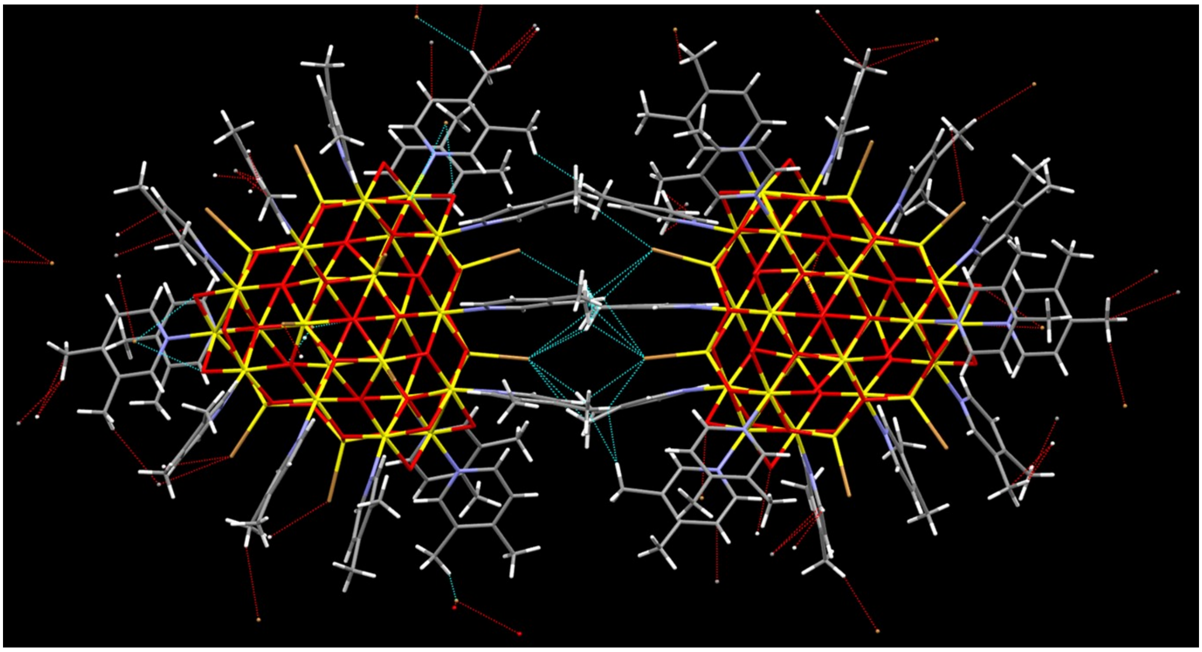

Figure S2. Closest intermolecular interactions in **1** between the lut molecules and Br ions, highlighted by the dashed blue lines at C···C/Br distances of ≥ 3.2 Å.

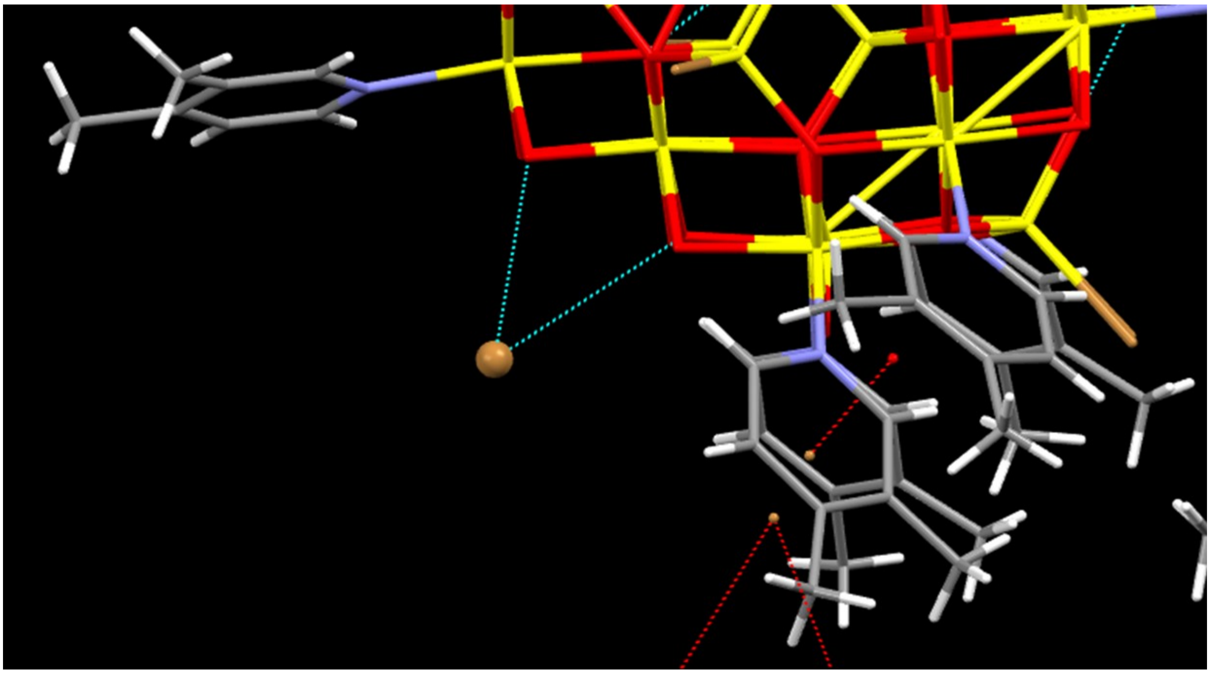

Figure S3. Close-up of the H-bond between a Br counter anion and the μ-OH ions the cluster.

Mass Spectrometry

Mass spectrometry was performed on a 7 T SolariXr FT-ICR MS (Bruker Daltonics, Bremen, Germany) with an ESI source. The spectrum was acquired in positive ion mode (ESI+). The broadband spectrum was acquired with 16 summed scans between 101 - 6000 *m/z*. Samples were solubilized in a 20/80 3,4-lutidine/acetonitrile mix at 230 µM and sprayed by direct infusion into the ESI source. Data were analysed using Bruker Compass DataAnalysis software. Time resolved mass spectrometry was performed on the preparatory mixture used to make **1**, under the same conditions as the re-dissolved crystalline sample. Aliquots of the reaction were taken at *t* = 0, *t* = 2 hours and *t* = 4 hours. The latter spectrum was measured after filtering the solution to remove some precipitated material. Aliquots were diluted to 230 µM (*wrt* $FeBr_3$) with a 20/80 mix of 3,4-lutidine and acetonitrile.

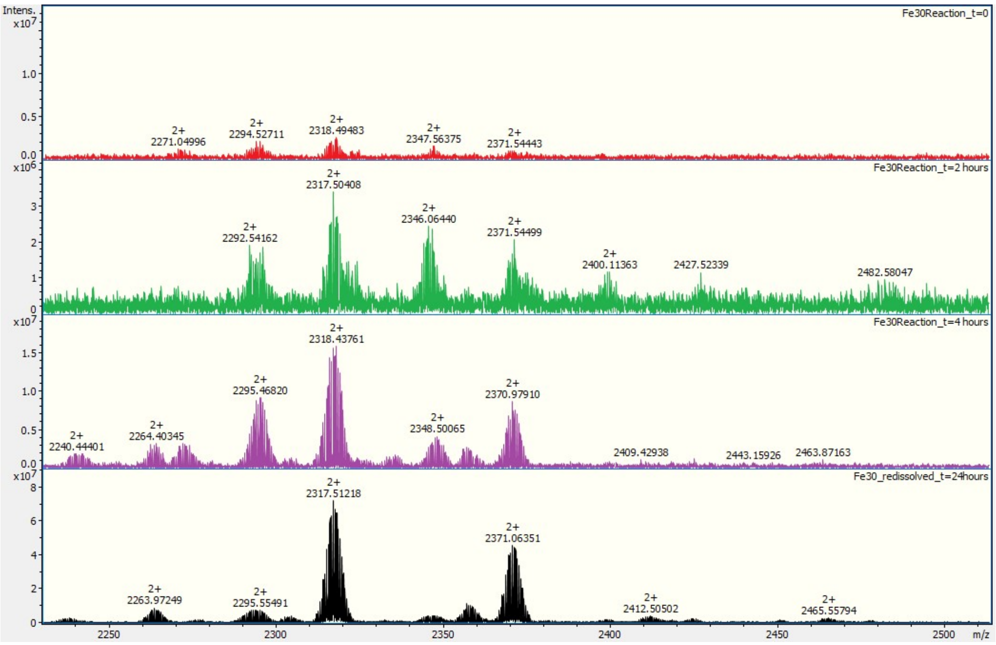

Figure S4. Time resolved mass spectra of the initial reaction mixture used to make compound **1** showing the characteristic peaks for [Fe_{30}] at 2317 and 2371 *m/z* at *t* = 0 (red); *t* = 2 hours (green); *t* = 4 hours (purple). The mass spectrum of crystalline **1** re-dissolved in a 20/80 mix of lut/MeCN (black) is shown for comparison.

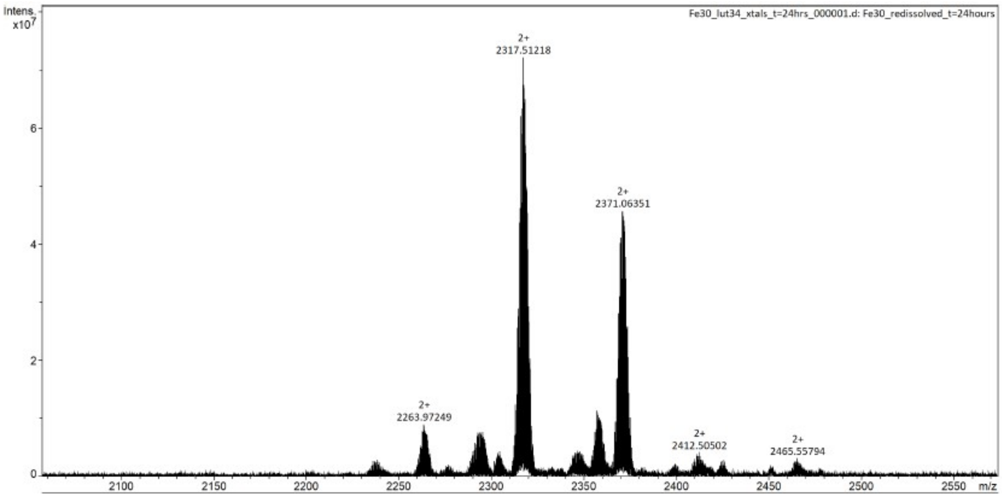

Figure S5. Mass spectrum of crystals of compound **1** re-dissolved in a 20/80 mix of lut/MeCN. The most intense peaks correspond to [[Fe_{30}]-(lut)+2(MeCN)]$^{2+}$ and [[Fe_{30}]-2(lut)+2(MeCN)]$^{2+}$ (2317 and 2371 *m/z* respectively). Less intense peaks correspond to fragments and adducts of [Fe30] and common MS impurities, including [[Fe_{30}]-3(lut)+2(MeCN)]$^{2+}$ (*m/z* = 2263), [[Fe_{30}]-2(lut)+2(H_2O)]$^{2+}$ (*m/z* = 2295) and [[Fe_{30}]+(CH_3COCH_3)]$^{2+}$ (*m/z* = 2412).

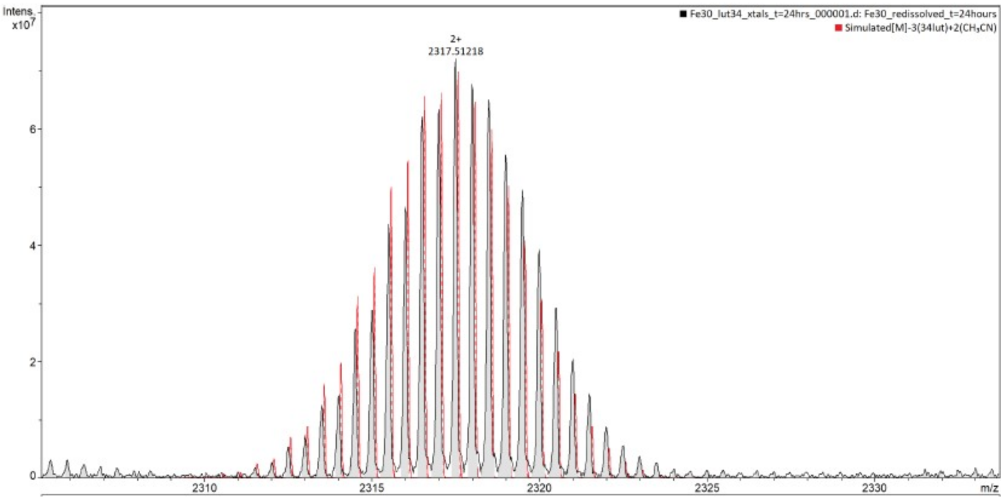

Figure S6. Mass spectrum highlighting the [[Fe_{30}]-(lut)+2(MeCN)]$^{2+}$ ion at *m/z* = 2317. The experimental data is in grey and the simulation in red.

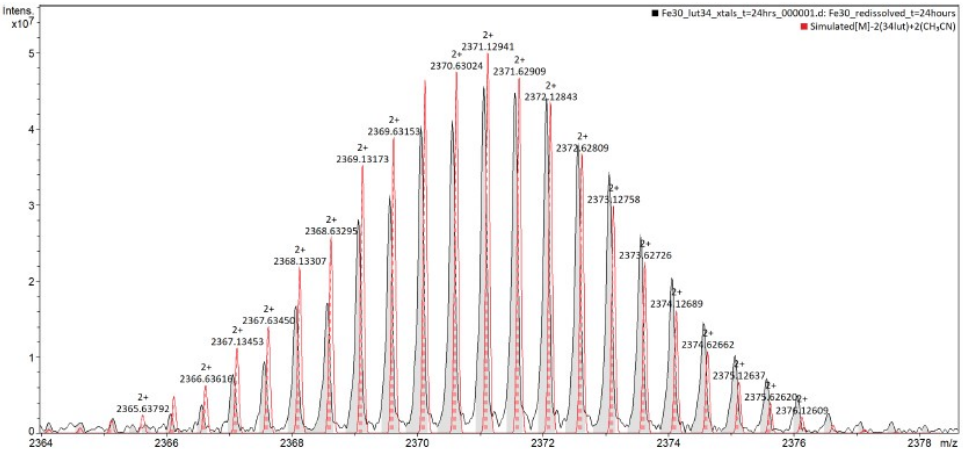

Figure S7. Mass spectrum highlighting the [[Fe_{30}]-2(lut)+2(MeCN)]$^{2+}$ ion at *m*/*z* = 2371. The experimental data is in grey and the simulation in red.

Computational Details

DFT calculations have been performed with the B3LYP functional using the Gaussian09 suite of programs.[3-6] The B3LYP functional is well known to provide excellent numerical accuracy in the estimation of magnetic exchange interaction values.[7,8] Here, we have estimated the pairwise exchange interactions using nine truncated models (Figure S9) as the DFT calculation is computationally expensive with complete structure of **1**. These models were constructed without altering the first coordination sphere of each pair of Fe^{III} centres, substituting neighbouring Fe^{III} sites with diamagnetic Ga^{III} ions. OH/H_2O moieties were employed for the truncated O atoms. Ahlrichs' triple-ξ plus polarisation basis set (TZVP) was used for the Fe, O, N, Br atoms and the split valence plus polarisation (SVP) basis set was used for the Ga, C and H atoms.[8] One high spin (HS, the electrons in the two Fe^{III} centres are "spin up") and one broken symmetry (BS, the electrons in one Fe(III) centre are "spin up", while those in the other are "spin down") configuration were considered for the exchange interaction, estimated using Noodleman's approach (spin-Hamiltonian (1) and (2)).[9,10] We have used the formula $J = \dfrac{E_{BS} - E_{HS}}{2S_1S_2 + S_2}$ for the estimation of nine pairwise exchange interactions $J_1, J_2, J_2^{'}, J_3, J_3^{'}, J_3^{''}, J_4, J_5$ and $J_5^{'}$.

The following spin-Hamiltonian has been employed for the estimation of exchange coupling constant in **1**.

$$\begin{aligned}\hat{H} &= -J_1\left[\hat{S}_1\hat{S}_2 + \hat{S}_1\hat{S}_3 + \hat{S}_2\hat{S}_3\right] - J_2\left[\hat{S}_1\hat{S}_4 + \hat{S}_1\hat{S}_{18} + \hat{S}_1\hat{S}_{17} + \hat{S}_1\hat{S}_{23} + \hat{S}_1\hat{S}_{25} + \hat{S}_1\hat{S}_{26} + \hat{S}_2\hat{S}_5 + \hat{S}_2\hat{S}_7 +\right. \\ &- J_3 \\ &\left[\hat{S}_{29}\hat{S}_{26} + \hat{S}_{26}\hat{S}_{25} + \hat{S}_{25}\hat{S}_{23} + \hat{S}_{25}\hat{S}_{18} + \hat{S}_{18}\hat{S}_{23} + \hat{S}_{23}\hat{S}_4 + \hat{S}_4\hat{S}_5 + \hat{S}_5\hat{S}_7 + \hat{S}_5\hat{S}_{22} + \hat{S}_7\hat{S}_{22} + \hat{S}_{22}\hat{S}_{21} +\right. \\ &- J_4\left[\hat{S}_{19}\hat{S}_{20} + \hat{S}_6\hat{S}_{24} + \hat{S}_6\hat{S}_{30} + \hat{S}_{24}\hat{S}_{30} + \hat{S}_{27}\hat{S}_{28} + \hat{S}_{11}\hat{S}_{12}\right] - J_5 \\ &\left[\hat{S}_{12}\hat{S}_{21} + \hat{S}_{12}\hat{S}_{22} + \hat{S}_{12}\hat{S}_7 + \hat{S}_{12}\hat{S}_8 + \hat{S}_{11}\hat{S}_8 + \hat{S}_{11}\hat{S}_9 + \hat{S}_{11}\hat{S}_{10} + \hat{S}_{11}\hat{S}_{14} + \hat{S}_{19}\hat{S}_4 + \hat{S}_{19}\hat{S}_{23} + \hat{S}_{19}\hat{S}_{17}\right. \\ &- J_2^{'}\left[\hat{S}_1\hat{S}_{15} + \hat{S}_1\hat{S}_{16} + \hat{S}_2\hat{S}_{13} + \hat{S}_2\hat{S}_{16} + \hat{S}_3\hat{S}_{13} + \hat{S}_3\hat{S}_{15}\right] - J_3^{'} \\ &\left[\hat{S}_{13}\hat{S}_{16} + \hat{S}_{13}\hat{S}_{15} + \hat{S}_{15}\hat{S}_{16} + \hat{S}_{13}\hat{S}_{14} + \hat{S}_{13}\hat{S}_{21} + \hat{S}_{16}\hat{S}_{21} + \hat{S}_{16}\hat{S}_{17} + \hat{S}_{15}\hat{S}_{17} + \hat{S}_{15}\hat{S}_{14}\right] - J_3^{''}[\hat{S}_{27} \\ &\hat{S}_{15} + \hat{S}_{27}\hat{S}_2 + \hat{S}_{26}\hat{S}_{10} + \hat{S}_{26}\hat{S}_8 + \hat{S}_{30}\hat{S}_{10} + \hat{S}_{30}\hat{S}_{15} +]J_5^{'}[\hat{S}_{12}\hat{S}_{13} + \hat{S}_{11}\hat{S}_{13} + \hat{S}_{15}\hat{S}_{27} + \hat{S}_{15}\hat{S}_{28} \\ &+ \hat{S}_{16}\hat{S}_{19} + \hat{S}_{16}\hat{S}_{20}]\end{aligned}$$

………………(1)

The above Hamiltonian can be simplified as

$$\begin{aligned}\hat{H} &= -3J_1\left[\hat{S}_{ITd}\hat{S}_{ITd}\right] - 18J_2\left[\hat{S}_{ITd}\hat{S}_{oct}\right] - 6J_2^{'}\left[\hat{S}_{ITd}\hat{S}_{oct}\right] - 18J_3\left[\hat{S}_{oct}\hat{S}_{oct}\right] - 9J_3^{'}\left[\hat{S}_{oct}\hat{S}_{oct}\right] - 6J_3^{''}\left[\hat{S}_{oct}\hat{S}_{oct}\right] \\ &- 37J_5\left[\hat{S}_{OTd}\hat{S}_{oct}\right] - 6J_5^{'}\left[\hat{S}_{OTd}\hat{S}_{oct}\right]\end{aligned}$$

…………..(2)

Where ITd, OTd and oct denote the inner tetrahedral, outer tetrahedral and octahedral Fe^{III} centres, respectively.

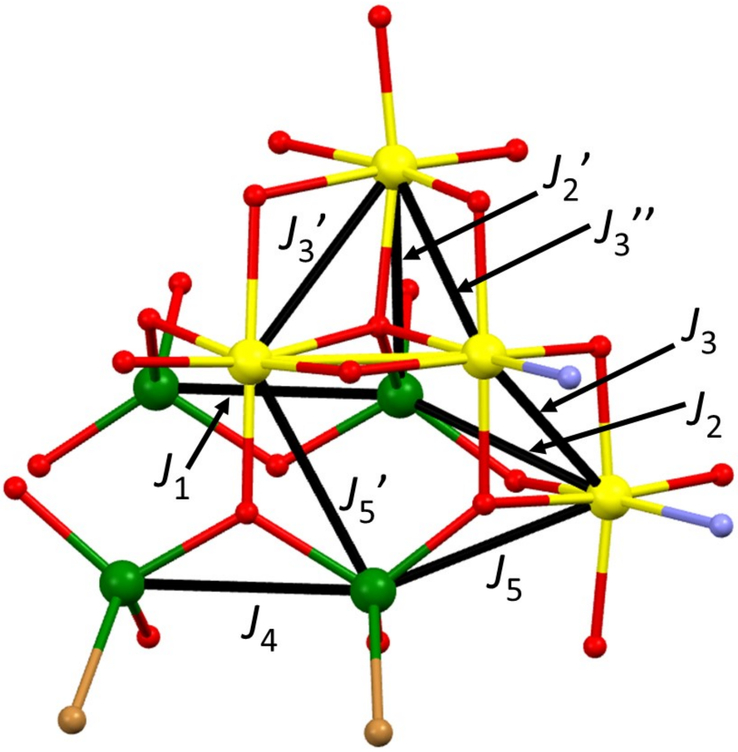

Scheme S1. Pictorial representation of the nine different magnetic exchange interactions in **1**.

	Fe-O-Fe (°)	Fe-O (Å)	Fe···Fe (Å)	J_{DFT}/ cm^{-1}
J_1	117.5	1.88	3.17	-30.6
J_2	121.2	1.93	3.36	-6.3
$J_2^{'}$	122.7	1.96	3.45	-19.2
J_3	94.9	1.97	2.92	-7.3
$J_3^{'}$	98.9	2.12	3.29	+14.3
$J_3^{''}$	99.6	2.00	3.05	-14.0
J_4	118.8	1.91	3.28	-60.0
J_5	130.3	1.89	3.44	-70.9
$J_5^{'}$	119.1	1.97	3.40	-24.9

Table S2. The nine DFT computed magnetic exchange interactions alongside the average Fe-O-Fe angles and average Fe-O and Fe···Fe distances for each interaction.

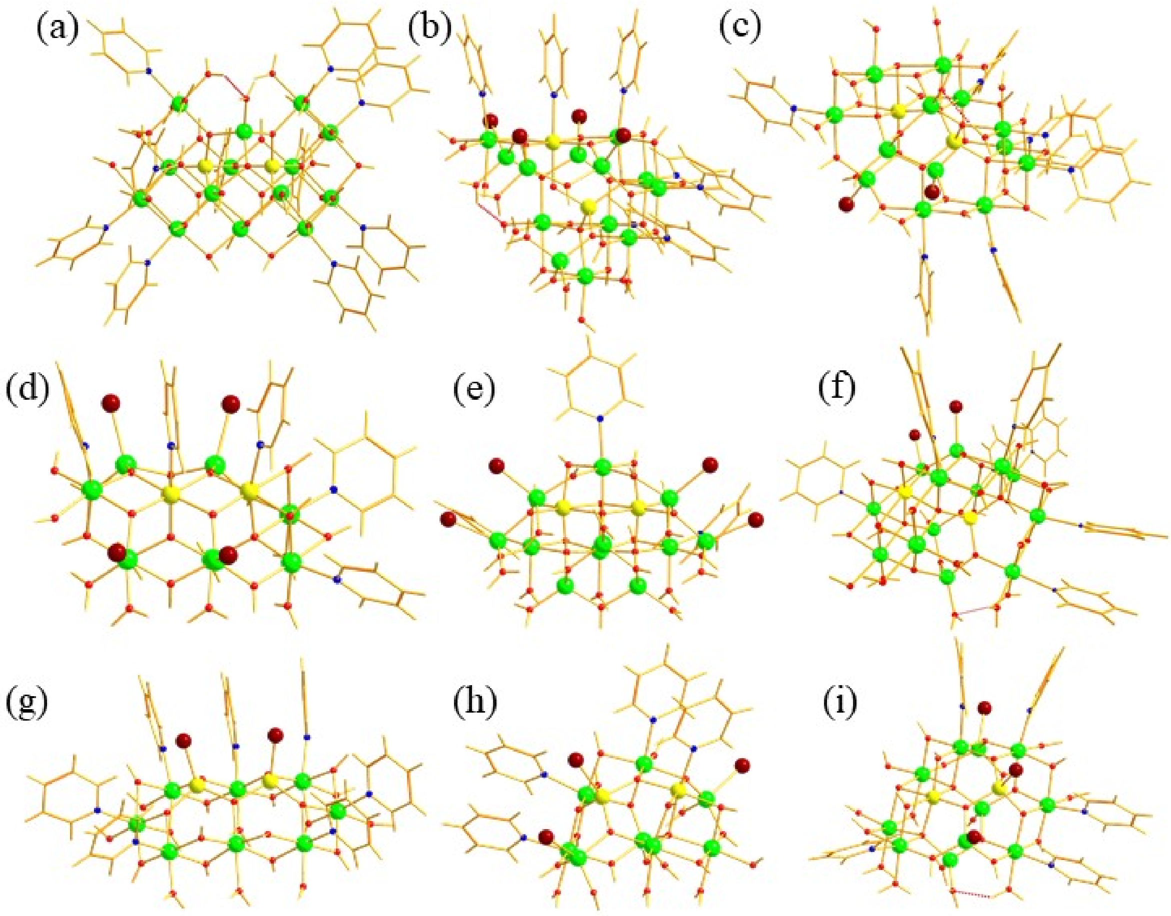

Figure S9. The nine models employed to estimate the magnetic exchange interactions in (a) J_1 (b) J_2 (c) J_2' (d) J_3 (e) J_3' (f) J_3'' (g) J_4 (h) J_5 (i) J_5' exchange pathway. Colour Code: Fe – Yellow; Ga – Green; Br - Brown; O – Red; N – Blue; C – Black, H – white.

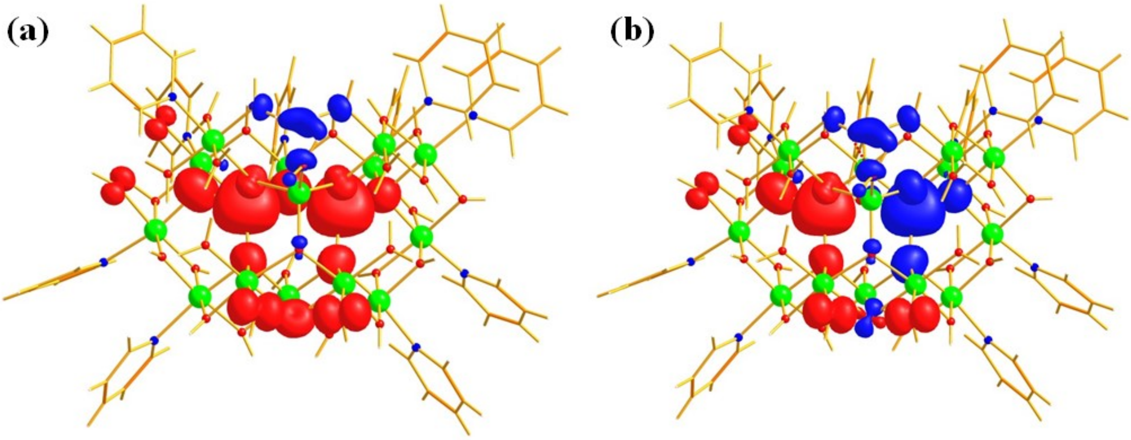

Figure S10. Spin density of the (a) HS (b) BS configurations of the model complex in the J_1 exchange pathway. The isodensity surface shown corresponds to a value of 0.006 e^-/bohr^3. The red and blue surfaces represent positive and negative spin density, respectively. Colour Code: Fe – Yellow; Ga – Green; Br - Brown; O – Red; N – Blue; C – Black, H – white.

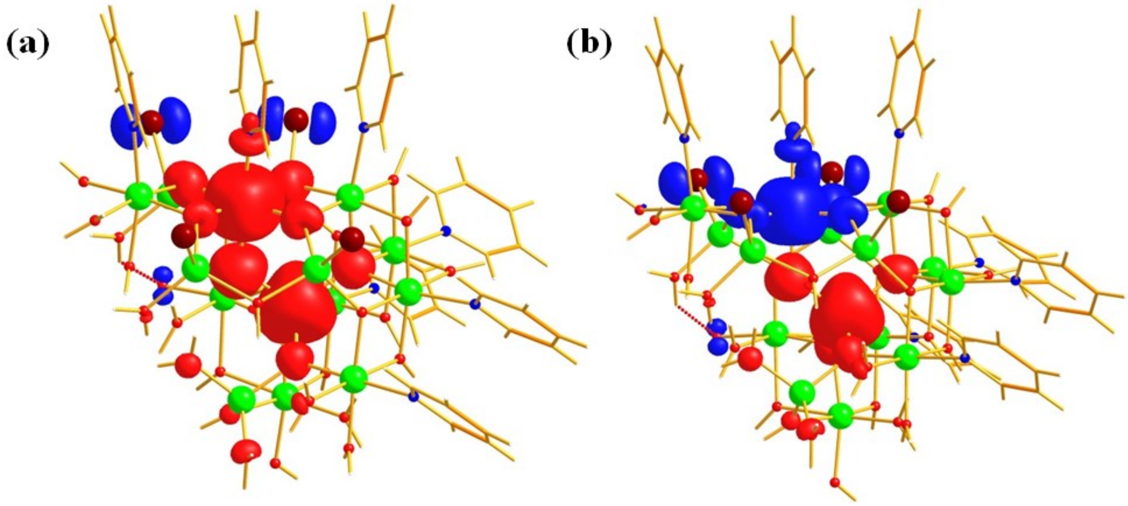

Figure S11. Spin density of the (a) HS (b) BS configurations of the model complex in the J_2 exchange pathway. The isodensity surface shown corresponds to a value of 0.006 e^-/bohr^3. The red and blue surfaces represent positive and negative spin density, respectively. Colour Code: Fe – Yellow; Ga – Green; Br - Brown; O – Red; N – Blue; C – Black, H – white.

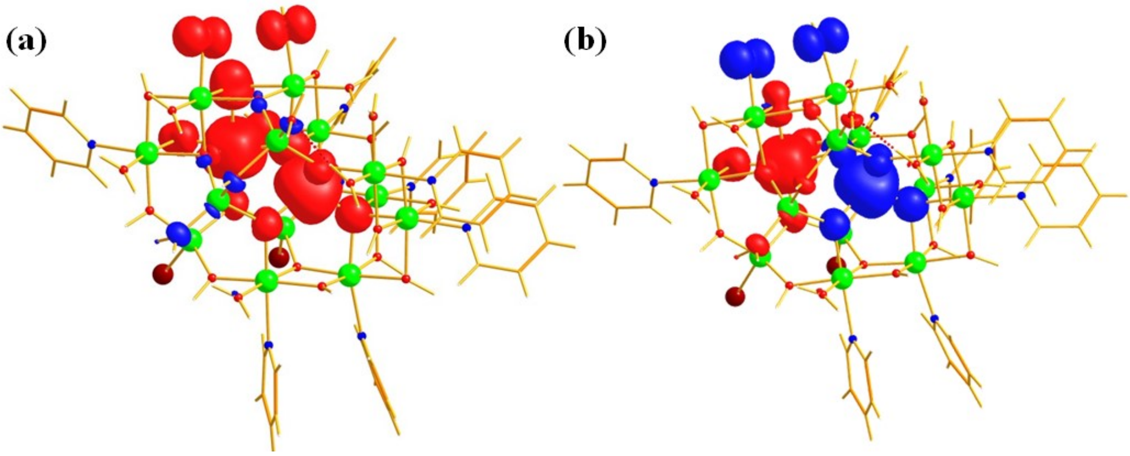

Figure S12. Spin density of the (a) HS (b) BS configurations of the model complex in the J_2' exchange pathway. The isodensity surface shown corresponds to a value of 0.006 e$^-$/bohr^3. The red and blue surfaces represent positive and negative spin density, respectively. Colour Code: Fe – Yellow; Ga – Green; Br - Brown; O – Red; N – Blue; C – Black, H – white.

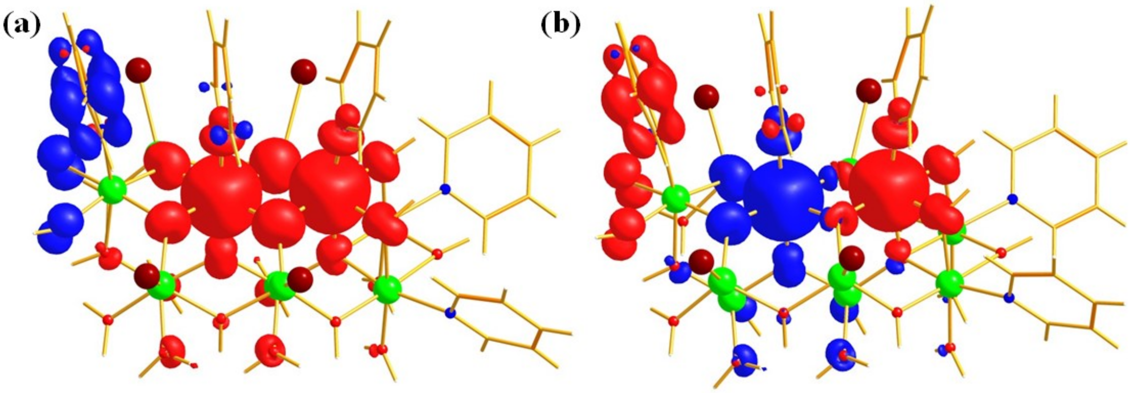

Figure S13. Spin density of the (a) HS (b) BS configurations of the model complex in the J_3 exchange pathway. The isodensity surface shown corresponds to a value of 0.006 e$^-$/bohr^3. The red and blue surfaces represent positive and negative spin density, respectively. Colour Code: Fe – Yellow; Ga – Green; Br - Brown; O – Red; N – Blue; C – Black, H – white.

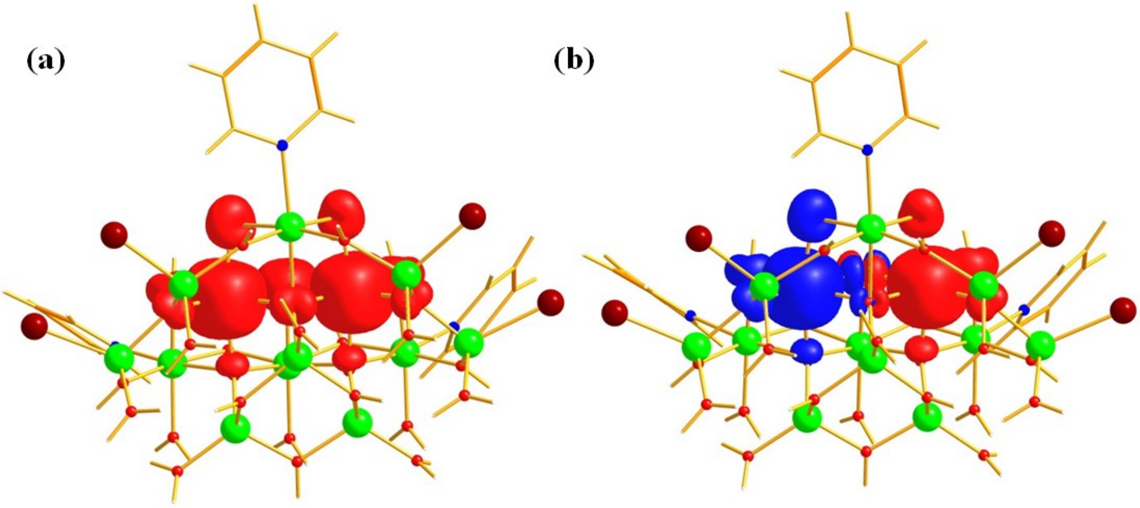

Figure S14. Spin density of the (a) HS (b) BS configurations of the model complex in the $J_3^{'}$ exchange pathway. The isodensity surface shown corresponds to a value of 0.006 e^-/bohr^3. The red and blue surfaces represent positive and negative spin density, respectively. Colour Code: Fe – Yellow; Ga – Green; Br - Brown; O – Red; N – Blue; C – Black, H – white.

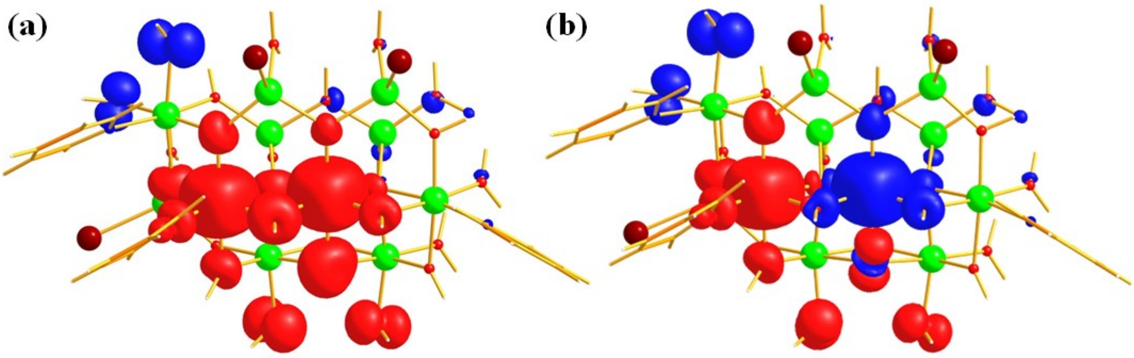

Figure S15. Spin density of the (a) HS (b) BS configurations of the model complex in the $J_3^{''}$ exchange pathway. The isodensity surface shown corresponds to a value of 0.006 e^-/bohr^3. The red and blue surfaces represent positive and negative spin density, respectively. Colour Code: Fe – Yellow; Ga – Green; Br - Brown; O – Red; N – Blue; C – Black, H – white.

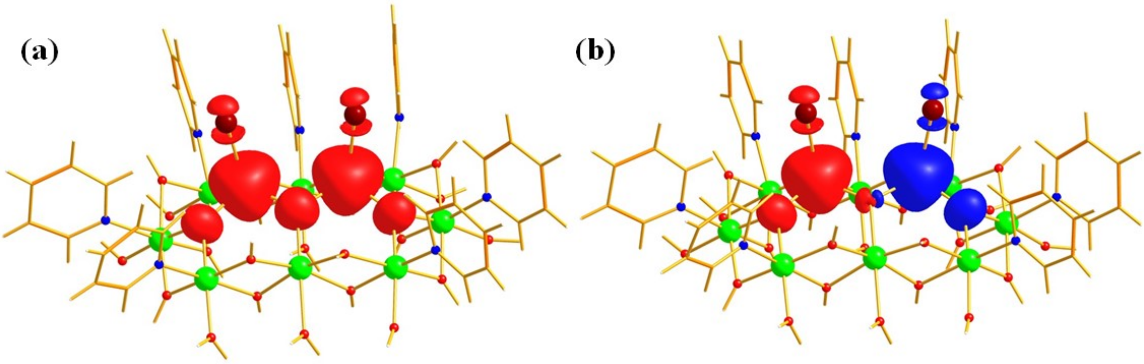

Figure S16. Spin density of the (a) HS (b) BS configurations of the model complex in the J_4 exchange pathway. The isodensity surface shown corresponds to a value of 0.006 e$^-$/bohr^3. The red and blue surfaces represent positive and negative spin density, respectively. Colour Code: Fe – Yellow; Ga – Green; Br - Brown; O – Red; N – Blue; C – Black, H – white.

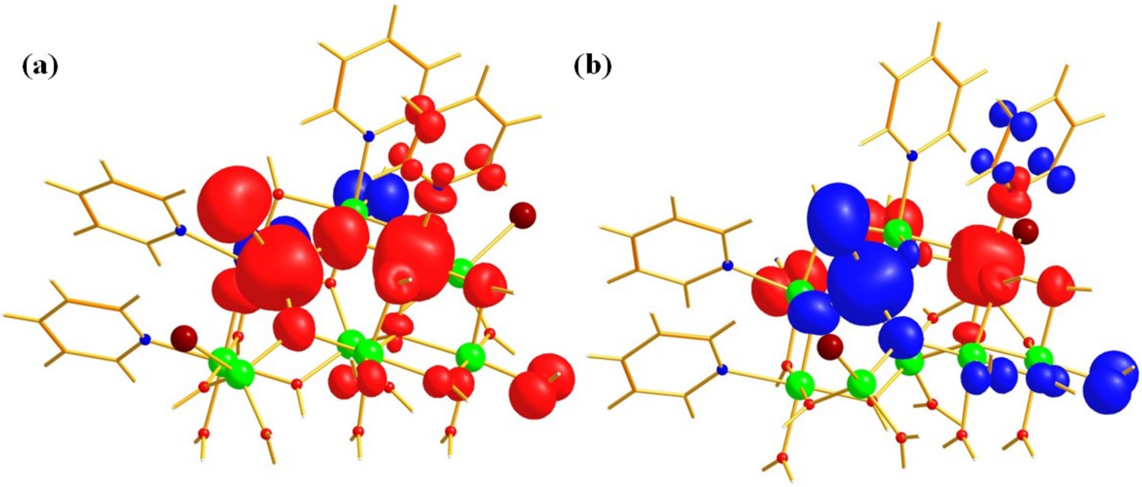

Figure S17. Spin density of the (a) HS (b) BS configurations of the model complex in the J_5 exchange pathway. The isodensity surface shown corresponds to a value of 0.006 e$^-$/bohr^3. The red and blue surfaces represent positive and negative spin density, respectively. Colour Code: Fe – Yellow; Ga – Green; Br - Brown; O – Red; N – Blue; C – Black, H – white.

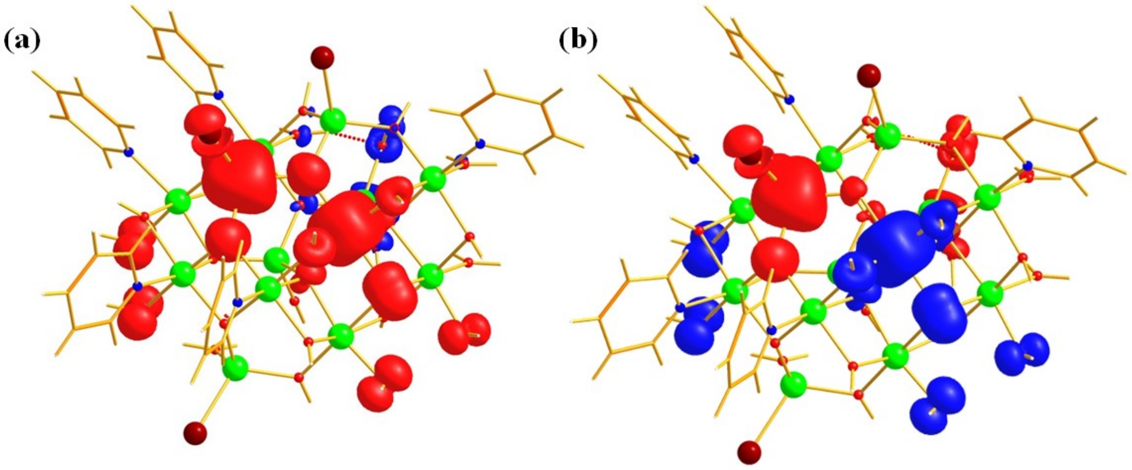

Figure S18. Spin density of the (a) HS (b) BS configurations of the model in the J_5' exchange pathway. The isodensity surface shown corresponds to a value of 0.006 e^-/bohr^3. The red and blue surfaces represent positive and negative spin density, respectively. Colour Code: Fe – Yellow; Ga – Green; Br - Brown; O – Red; N – Blue; C – Black, H – white

Table S3. Overlap integrals between the SOMOs of the two Fe^{III} centres in the J_1 exchange pathway.

Beta→ Alpha↓	d_{z2}	d_{xz}	d_{yz}	d_{x2-y2}	d_{xy}
d_{xz}	-0.122	0.132	-0.216	-0.223	0.095
d_{yz}	0.030	0.057	0.040	0.108	-0.071
d_{x2-y2}	-0.048	0.013	-0.012	0.236	-0.028
d_{xy}	0.026	-0.081	0.018	0.042	-0.029
d_{z2}	-0.007	0.121	0.046	0.017	-0.038

Table S4. Overlap integrals between the SOMOs of the two Fe^{III} centres in the J_2 exchange pathway.

Beta→ Alpha↓	d_{z2}	d_{yz}	d_{xz}	d_{x2-y2}	d_{xy}
d_{z2}	-0.010	-0.179	-0.019	-0.018	-0.029
d_{yz}	-0.018	-0.069	0.114	0.176	0.080
d_{xz}	-0.001	0.058	-0.012	-0.002	-0.062
d_{x2-y2}	0.030	0.268	-0.036	0.162	-0.025
d_{xy}	0.050	-0.017	-0.051	-0.019	0.232

Table S5. Overlap integrals between the SOMOs of the two Fe^{III} centres in J_2' exchange pathway.

Beta→ Alpha↓	d_{z2}	d_{yz}	d_{xz}	d_{x2-y2}	d_{xy}
d_{z2}	-0.059	0.111	-0.090	0.037	-0.022
d_{yz}	-0.137	-0.091	-0.192	0.068	0.028
d_{xz}	0.120	0.044	-0.002	0.022	-0.018
d_{x2-y2}	0.098	0.062	-0.041	-0.026	-0.019
d_{xy}	-0.227	-0.168	0.002	0.130	-0.060

Table S6. Overlap integrals between the SOMOs of the two Fe^{III} centres in the J_3 exchange pathway.

Beta→ Alpha↓	d_{xy}	d_{x2-y2}	d_{xz}	d_{z2}	d_{yz}
d_{z2}	-0.138	0.259	0.144	-0.080	0.046
d_{yz}	0.104	-0.216	0.138	0.014	-0.045
d_{xz}	0.241	0.091	-0.104	0.055	0.057
d_{x2-y2}	0.198	0.187	-0.149	0.122	-0.025
d_{xy}	0.012	0.140	-0.110	-0.078	-0.081

Table S7. Overlap integrals between the SOMOs of the two Fe^{III} centres in the J_3' exchange pathway.

Beta→ Alpha↓	d_{yz}	d_{x2-y2}	d_{xz}	d_{xy}	d_{z2}
d_{yz}	-0.006	-0.049	0.069	-0.017	-0.065
d_{xz}	0.107	0.086	-0.056	0.028	-0.159
d_{x2-y2}	0.040	0.049	-0.101	-0.192	-0.040
d_{xy}	-0.152	-0.077	-0.113	0.185	-0.048
d_{z2}	-0.128	-0.041	-0.123	0.058	-0.261

Table S8. Overlap integrals between the SOMOs of the two Fe^{III} centres in the J_3'' exchange pathway.

Beta→ Alpha↓	d_{z2}	d_{yz}	d_{xz}	d_{x2-y2}	d_{xy}
d_{z2}	0.326	0.013	-0.091	0.033	0.079
d_{yz}	0.211	0.001	-0.161	0.090	0.040
d_{xz}	0.074	-0.006	-0.098	-0.297	-0.003
d_{x2-y2}	-0.037	-0.071	0.139	0.057	-0.125
d_{xy}	-0.095	-0.000	-0.016	-0.140	0.009

Table S9. Overlap integrals between the SOMOs of the two Fe^{III} centres in the J_4 exchange pathway.

Beta→ Alpha↓	d_{xy}	d_{x2-y2}	d_{xz}	d_{yz}	d_{z2}
d_{xy}	0.189	0.204	-0.084	0.045	-0.053
d_{x2-y2}	-0.140	-0.050	-0.036	0.099	0.024
d_{xz}	0.365	0.038	0.022	0.068	0.081
d_{z2}	0.027	0.163	0.014	0.053	-0.075
d_{yz}	0.217	0.039	-0.236	0.003	0.099

Table S10. Overlap integrals between the SOMOs of the two Fe^{III} centres in the J_5 exchange pathway.

Beta→ Alpha↓	d_{x2-y2}	d_{xy}	d_{z2}	d_{xz}	d_{yz}
d_{xy}	-0.037	0.285	0.014	0.001	-0.066
d_{yz}	0.116	-0.043	-0.107	-0.099	-0.162
d_{x2-y2}	0.071	-0.180	0.103	-0.051	-0.102
d_{xz}	-0.221	-0.188	-0.099	-0.236	0.043

d_{z2}	0.174	0.148	0.014	-0.132	-0.126

Table S11. Overlap integrals between the SOMOs of the two Fe^{III} centres in the J_5' exchange pathway.

Beta→ Alpha↓	d_{z2}	d_{yz}	d_{xz}	d_{xy}	d_{x2-y2}
d_{z2}	-0.096	0.046	0.109	0.010	0.010
d_{yz}	0.070	0.044	-0.002	-0.018	0.022
d_{xz}	0.145	0.091	-0.192	0.028	0.068
d_{xy}	-0.087	-0.168	0.002	-0.060	0.130
d_{x2-y2}	0.203	0.062	-0.041	-0.019	-0.026

References

1. G. M. Sheldrick, *Acta Crystallogr. Sect. C: Cryst. Struct. Commun.,* 2015, **71**, 3-8.
2. O. V. Dolomanov, L. J. Bourhis, R. J. Gildea, J. A. K. Howard and H. Puschmann, *J. Appl. Crystallogr.* 2009, **42**, 339-341.
3. M. J. Frisch, G. W. Trucks, H. B. Schlegel, G. E. Scuseria, M. A. Robb, J. R. Cheeseman, G. Scalmani, V. Barone, G. A. Petersson, H. Nakatsuji, X. Li, M. Caricato, A. Marenich, J. Bloino, B. G. Janesko, R. Gomperts, B. Mennucci, H. P. Hratchian, J. V. Ortiz, A. F. Izmaylov, J. L. Sonnenberg, D. Williams-Young, F. Ding, F. Lipparini, F. Egidi, J. Goings, B. Peng, A. Petrone, T. Henderson, D. Ranasinghe, V. G. Zakrzewski, J. Gao, N. Rega, G. Zheng, W. Liang, M. Hada, M. Ehara, K. Toyota, R. Fukuda, J. Hasegawa, M. Ishida, T. Nakajima, Y. Honda, O. Kitao, H. Nakai, T. Vreven, K. Throssell, J. A. Montgomery Jr., J. E. Peralta, F. Ogliaro, M. Bearpark, J. J. Heyd, E. Brothers, K. N. Kudin, V. N. Staroverov, T. Keith, R. Kobayashi, J. Normand, K. Raghavachari, A. Rendell, J. C. Burant, S. S. Iyengar, J. Tomasi, M. Cossi, J. M. Millam, M. Klene, C. Adamo, R. Cammi, J. W. Ochterski, R. L. Martin, K. Morokuma, O. Farkas, J. B. Foresman, D. J. Fox, Gaussian 09, Revision A.02, Gaussian Inc., Wallingford CT, 2016.
4. D. Becke, *J. Chem. Phys*., 1993, **98**, 5648–5652.
5. A. Schäfer, H. Horn and R. Ahlrichs, *J. Chem. Phys*., 1992, **97**, 2571–2577.
6. A. Schäfer, C. Huber and R. Ahlrichs, *J. Chem. Phys*., 1994, **100**, 5829–5835.
7. H. W. L. Fraser, L. Smythe, S. Dey, G. S. Nichol, S. Piligkos, G. Rajaraman, E. K. Brechin, *Dalton Trans*., 2018 , **47**, 8100-8109.
8. M. M. Hänninen, A. J. Mota, R. Sillanpää, S. Dey, G. Velmurugan, G. Rajaraman and E. Colacio, *Inorg. Chem*., 2018, **57**, 3683–3698.
9. L. Noodleman, *J. Chem. Phys*., 1981, **74**, 5737–5743.
10. E. Ruiz, J. Cano, S. Alvarez and P. Alemany, *J. Comput. Chem*., 1999, **20**, 1391-1400.